Carrier density and quantum capacitance for semiconducting carbon nanotubes

Jiale Liang, Deji Akinwande, and H.-S. Philip Wong

Citation: Journal of Applied Physics **104**, 064515 (2008); doi: 10.1063/1.2986216
View online: http://dx.doi.org/10.1063/1.2986216
View Table of Contents: http://aip.scitation.org/toc/jap/104/6
Published by the American Institute of Physics

Carrier density and quantum capacitance for semiconducting carbon nanotubes

Jiale Liang,[a] Deji Akinwande,[b] and H.-S. Philip Wong[c]
Center for Integrated Systems and Department of Electrical Engineering, Stanford University, Stanford, California 94305, USA

(Received 26 June 2008; accepted 6 August 2008; published online 29 September 2008)

A full-band analytical model of the equilibrium carrier density for single-wall semiconducting carbon nanotubes (sCNTs) is presented. The carrier density, which is a fundamental property of all semiconductors, is obtained using a semiempirical method for degenerate positions of the Fermi level and shows good agreement with numerical tight-binding results. The quantum capacitance is subsequently derived from the carrier density and used to develop a C-V model with good agreement with experimental quantum capacitance measurements. An analytical model of the gate coupling function of sCNTs is also reported which relates the internal surface potential with the external applied gate voltage. The diameter temperature and Fermi level dependency, and the essential properties of carbon nanotubes device physics are captured in these analytical equations.
 [DOI: 10.1063/1.2986216]

I. INTRODUCTION

Carbon nanotubes (CNTs) are quasi one-dimensional (1D) solids that exhibit fascinating properties such as ballistic transport in transistors and interconnects, van Hove singularities (VHS), which are of key interest in spectroscopy, and selective functionalization for sensing applications.[1–5] To gain physical insights into the electrical properties of CNT devices, it is imperative that the device physics be routinely accessible through intuitive analytical equations. A fundamental parameter to describe the device physics and transport of electrons and holes in a semiconductor is the carrier density.[6] In semiconducting carbon nanotubes (sCNTs), the carrier density is often computed from numerical integration of the density of states (DOS) and the Fermi–Dirac distribution because of the nonanalyticity of the integrand.[7] However, the numerical computation clouds insight into the device physics and does not provide a transparent guide as to how to optimize the nanotube for the desired performance. In addition, basic current-voltage (*I-V*) and capacitance-voltage (C-V) numerical simulations, which although are accurate and useful, are nonetheless, time consuming for the development of compact device models for fast circuit simulations.

In this article, we describe a semiempirical analytical equation for the degenerate equilibrium carrier density for electrons and holes specifically for zigzag sCNTs. The analytical equations are in good agreement ($<8\%$ error) compared to numerical nearest neighbor tight-binding (NNTB) computation for arbitrary positions of the Fermi level below the bottom of the second subband which determines transport in practical CNT devices.[7,8] In addition, we derive the degenerate quantum capacitance from the carrier density, which is used to develop a model for the C-V of a top-gated CNT device showing good agreement with experimental CNT quantum capacitance measurements.[9] At the same time, we present an analytical coupling function that quantifies how the external gate voltage couples onto the internal surface potential of the CNT. The gate coupling function includes the essential 1D electrostatics that at low energies the quantum capacitance dominates over the gate oxide capacitance and vice versa at high energies.

The equilibrium carrier density and quantum capacitance are useful in describing low energy transport in the ballistic and semiclassical regime where the Fermi–Dirac distribution is a good approximation to the nonequilibrium distribution function. This approximation is known as the quasiequilibrium approximation and is widely employed in conventional semiconductors. Also, the analytical equations can be utilized in the development of compact models for device and circuit simulations.[10–12] The results derived in this paper for zigzag sCNTs are generally applicable to chiral sCNTs with similar diameters for low energies due to the strong diameter dependence of the low energy bandstructure.[13,14] The accuracy of the analytical model described in this work is strongly dependent on the validity of the NNTB formalism, which is very accurate in describing the lowest subbands for CNTs with diameters ≥ 1 nm, where curvature effects and sigma-pi hybridization are negligible.[15–17] Fortunately, most practical electronic applications of CNTs are within the validity of the NNTB theory making the analytical model valuable for CNT device physics.

II. ANALYTICAL CARRIER DENSITY

A. Carrier density calculation

In this section, we describe the analytical carrier density for sCNTs. Although the calculation is for the electron carrier density (conduction band), it also applies equally to holes (valence band) due to electron-hole symmetry in the lowest subbands for CNTs.[9,18] The electron carrier density (n) is formally given by

[a]Electronic mail: liangjl@stanford.edu.
[b]Electronic mail: dejia@stanford.edu.
[c]Electronic mail: hspwong@stanford.edu.

$$n = \int_{E_{cb}(q)}^{E_{ct}(q)} F(E,E_F) \sum_q g_{zz}(E,q) dE, \quad (1)$$

where $F(E,E_F)$ is the Fermi–Dirac distribution, E_F is the Fermi energy or chemical potential, and E_{ct} and E_{cb} are the top and bottom of the conduction band (NNTB π^* band) of each subband, respectively. The intrinsic Fermi energy is 0 eV. The integration is over all the subbands indexed by q, and g_{zz} is the zigzag DOS contribution per subband for $E_{cb}(=E_{VH1}) \leq E \leq E_{ct}$:[8]

$$g_{zz}(E,q) = g_0 \gamma_0 \frac{|E|}{\sqrt{(E^2 - E_{VH1}^2)(E_{VH2}^2 - E^2)}}, \quad (2a)$$

$$g_0 = \frac{8}{\sqrt{3} a \pi \gamma_0}. \quad (2b)$$

E_{VH1} and E_{VH2} are the energies of the zigzag VHS which define the energy space where the DOS is real, and g_o is a CNT material constant, and also the ground state DOS for metallic CNTs.[16] γ_0 is the nearest neighbor overlap energy nominally between 2.5 and 3.2eV, and a is the graphene Bravais lattice constant (~2.46 Å).

In general, Eq. (1) does not have an exact analytical solution. However, for nondegenerate Fermi levels $[E_{cb}(q) - E_F > 3kT]$, a solution in terms of the modified Bessel function of the second kind has been recently derived for the nondegenerate carrier density ($n_{\_nd}$),[8]

$$n_{\_nd} = 2N_0 e^{\frac{E_F - E_{cb}}{kT}}, \quad (3a)$$

$$N_0 = g_0 \gamma_0 \frac{2E_{VH1} + kT}{4E_{VH2}} \sqrt{\frac{2\pi kT}{E_{VH1}}} \approx \frac{g_0}{4} \sqrt{\pi k T E_g}, \quad (3b)$$

where N_0 is the effective DOS and E_g is the band gap for each subband. Both N_0 and E_g are subband dependent. By substituting $E_{VH1} + kT/2 \approx E_g/2$ and $E_{VH2} \approx 2\gamma_0$,[8] N_0 is further simplified in Eq. (3b) to illustrate a relationship proportional with $T^{1/2}$. However, the actual carrier densities are determined by the Boltzmann exponential in Eq. (3a). In the analysis of carrier density for semiconducting CNTs developed in this paper, we use the exact value of N_0 without simplification.

In order to proceed further in evaluating Eq. (1) for the degenerate case, we will restrict the analysis to cover the range of Fermi level arbitrarily up to the bottom of the second subband $E_{cb}(q_2)$, as shown in Fig. 1, and for nanotube diameters ≥1 nm. This restriction is within the validity of the NNTB model and covers most electronic and semiconductor applications since in practical CNT transistors, E_F will not rise much beyond $E_{cb}(q_2)$.[7,8] Furthermore, due to the rapidly decaying Fermi exponential, high energy states are weakly populated and do not contribute appreciable numbers of carriers. The increase in the carrier density when including the contribution of the subbands with band index higher than 2 is ≪0.1%. In mathematical terms, this implies that the relevant energies are much smaller than the top of the second subband, and the summation of DOS over all subbands in Eq. (1) can be accurately reduced to include only the first and second subband. For clarity we call this restriction the two-subband approximation.

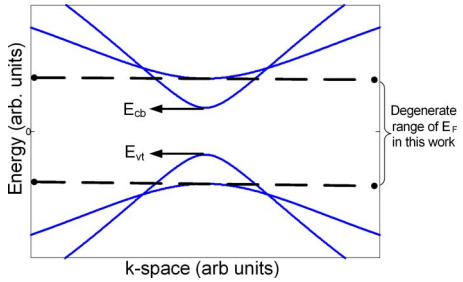

FIG. 1. (Color online) An illustrative plot of the band structure of CNT showing the first two subbands and the maximum variation of the Fermi level considered in this work.

Figure 2 shows an illustrative numerical solution to Eq. (1) for a typical subband. While the nondegenerate electron carrier density has a strict linear curve (in logarithmic scale) and a high slope, the degenerate case is quasilinear with a reduced slope. More precisely, the degenerate electron carrier density can be approximated by an *exponential power series* because the slope of $\log[n(q)]$ is not constant but gradually decreases with $(E_F - E_{cb})/kT$. The agreement between the numerical NNTB simulation and the exponential approximations with higher order terms is enlarged in the inset of Fig. 2.

Therefore, based on the nondegenerate carrier density [Eq. (3a)], and the exponential power series for the degenerate case, the electron carrier density per subband can be expressed as [for $E_F \leq E_{cb}(q_2)$]

$$n(q) = \frac{2N_0 e^{x_n}}{1 + A e^{\alpha x_n + \beta x_n^2 + \gamma x_n^3 + \kappa x_n^4 + \ldots + \zeta x_n^m}}, \quad x_n = \frac{E_F - E_{cb}}{kT}, \quad (4)$$

where A is a constant, α, β, γ, $\kappa \ldots \zeta$ are the weights of the power terms in Eq. (4), and x_n is the normalized energy

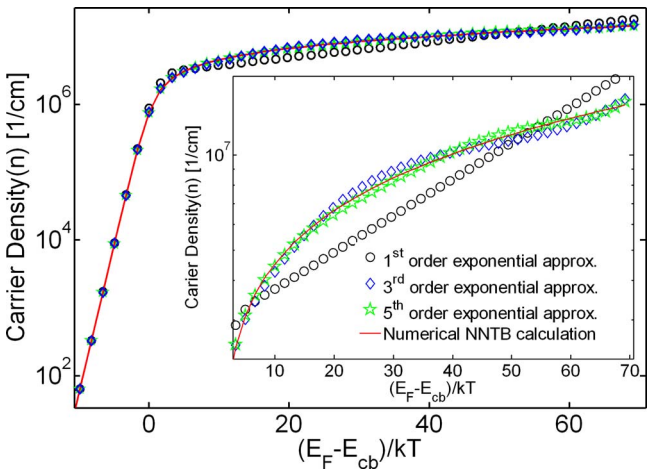

FIG. 2. (Color online) A numerical solution and exponential approximations with different orders for the electron carrier density (n) versus the normalized Fermi energy for a subband with 0.7eV band gap (d=1 nm). The carrier density is well approximated by two exponentials; one exponential describes the nondegenerate case (the steeper slope in the figure) and the other describes the degenerate case. The inset shows an enlarged view of the degenerate electron carrier density, making it visibly obvious that the higher order exponential approximations approach the numerical NNTB computation.

difference. The factor of 2 is for the subband degeneracy. It is clear that when E_F is $3kT$ lower than $E_{cb}(q)$, Eq. (4) reduces to the nondegenerate case. However, when the Fermi energy is degenerate $[E_F > E_{cb}(q) - 3kT]$, the exponential term in the denominator becomes the dominant factor, and the degenerate electron carrier density per subband is simply a power series in the logarithmic scale:

$$\ln[n(q)] \approx \ln\left(\frac{2N_0}{A}\right) + (1-\alpha)x_n - \beta x_n^2 - \gamma x_n^3 - \kappa x_n^4 - \ldots - \zeta x_n^m. \quad (5)$$

In the two-subband approximation, the total electron carrier density is obtained by summing up $n(q_1)$ and $n(q_2)$. Likewise, the hole carrier density (p) per subband can be expressed as

$$p(q) = \frac{2N_0 e^{x_p}}{1 + Ae^{\alpha x_p + \beta x_p^2 + \gamma x_p^3 + \kappa x_p^4 + \ldots + \zeta x_p^m}}, \quad x_p = \frac{E_{vt} - E_F}{kT}, \quad (6)$$

where E_{vt} is the top of the valence band (NNTB π band) for each subband, and x_p is the corresponding normalized energy difference. In the two-subband approximation, the total hole carrier density is obtained by summing up $p(q_1)$ and $p(q_2)$. Equations (4) and (6) and their subsequent application in deriving the quantum capacitance are the main results of this paper.

B. Accuracy of analytical carrier density

As expected, the accuracy of the model is dependent on the number of terms in the power series. In general, the values of the weights are band gap and temperature sensitive. In the two-subband approximation, the empirical-fitting range for electron carrier density is

$$x_{n\_\max} = \left(\frac{E_F - E_{cb}}{kT}\right)_{\max} = \frac{E_{cb}(q_2) - E_{cb}(q_1)}{kT_{\min}} \approx \frac{\gamma_0 a}{\sqrt{3}k(dT)_{\min}}, \quad (7a)$$

$$x_{n\_\min} = \left(\frac{E_F - E_{cb}}{kT}\right)_{\min} = -\frac{E_{cb}(q_2)}{kT_{\min}} \approx -\frac{2\gamma_0 a}{\sqrt{3}k(dT)_{\min}}. \quad (7b)$$

The range of the dT product in the model is from 70 to 1500 nm·K, which includes most practical application of CNTs, e.g., for a CNT with 2 nm diameter, the model is valid for CNT temperatures ranging from 35 to 750 K. The value of $x_{n\_\max}$ which is generally inversely proportional to the dT product is hence calculated to change roughly from 3 to 68 for semiconducting CNTs. The value of $x_{n\_\min}$ does not restrict the application range of our model since it is associated with the nondegenerate case.

In order to balance the trade-off between analytical complexity and accuracy, an effective way is to divide the dT product (directly related to the fitting range) into several regions, and determine the value of the weights for each region. We find up to three regions of the dT product are necessary in order to keep the error $<8\%$ while limiting the number of terms in the power series to three, namely, the high dT region (dT=220–1500 nm·K), the medium dT region (dT=150–220 nm·K), and the low dT region (dT=70–150 nm·K). It can be seen that for most CNT applications operating at room temperature for diameters from 1 to 4 nm the high dT region is the only relevant region.

Further analysis of the magnitude of the weights enables us to reduce the number of parameters in the model. The scale of the weight in the power series determines the range of x_n when the impact of higher order terms begins to be appreciable compared to the linear $(1-\alpha)$-term in Eq. (5). A rough estimation of the magnitude of the weights shows $1-\alpha$, β, γ, and κ are on orders of 0.1, 10^{-3}, 10^{-5}, and 10^{-7}, decreasing dramatically with the term orders. As a result, it is reasonable to neglect the contribution of higher order terms in the power series according to the fitting range for the simplification of the model. In the two-subband approximation with $x_{n\_\max} \approx 68$, we confine the expansion of the power series to the cubic γ-term in Eq. (5) for two subbands. We do not include κ-term for the sake of simplicity though its contribution begins to be appreciable for low dT region, which impairs the accuracy of this region a bit as we will show later. The simplified expression of the total electron carrier density can then be obtained by summing up the contribution of two subbands:

$$n \approx \sum_{q=1}^{2} n(q) \approx \sum_{q=1}^{2} \frac{2N_0 e^{x_n}}{1 + Ae^{\alpha x_n + \beta x_n^2 + \gamma x_n^3}}. \quad (8)$$

The values of the weights are determined by empirical-fitting to the numerical integration by minimizing the peak error and are assumed to be same for two subbands. This assumption is reasonable since the second subband is nondegenerate for most Fermi positions in the two-subband approximation and is hence insensitive to the choice of fitting weights. In fact, β and γ can be set to zero in the second subband for simplification, with negligible increase in the peak error.

Using the optimal values of the weight parameters (see Table I), the analytical electron carrier density [Eq. (8)] is in good agreement with the results of numerical integration. As mentioned before, the low dT region has a slightly larger value of peak error due to the neglect of the κ-term. Figure 3 shows the comparison between the numerical and analytical electron carrier density at room temperature for different CNT diameters with strong agreement. For further simplicity, we also present an analytical model with a second order exponential series for two subbands in the Appendix, still showing acceptable error.

Replacing x_n with x_p in Eq. (8), the simplified model and extracted optimal values of weight parameters also apply to describe the hole carrier density due to the electron-hole symmetry.[9,18] Therefore, the analytical hole carrier density per subband can be approximated as

$$p \approx \sum_{q=1}^{2} p(q) \approx \sum_{q=1}^{2} \frac{2N_0 e^{x_p}}{1 + Ae^{\alpha x_p + \beta x_p^2 + \gamma x_p^3}}. \quad (9)$$

A summary of the semiempirical model described above is given in Table I.

TABLE I. The characteristics and accuracy of the analytical model. The optimal values of A and weight parameters α, β, and γ for three regions are chosen to minimize the peak error for all regions. The high dT region is the only relevant region for practical CNTs with diameters from 1 to 4 nm operating at room temperature.

dT (nm·K)	Fitting weights α	β ($\times 10^{-3}$)	γ ($\times 10^{-5}$)	A	Peak error
70–150	0.91	1.55	−1.02	0.59	7.7%
150–220	0.88	3.57	−4.23	0.66	3.0%
220–1500	0.84	7.09	−12.30	0.71	4.3%

III. ANALYTICAL QUANTUM CAPACITANCE

The quantum capacitance per unit length (C_q), which is an essential parameter for CNT solid-state physics,[9] is determined by the derivative of the charge density:[19]

$$C_q(\varphi_s) = -\frac{\partial q_L}{\partial \varphi_s}, \tag{10a}$$

$$q_L = ep - en, \tag{10b}$$

where φ_s is the surface potential indicating how much the band moves up and down under an applied gate voltage and can be expressed as $e\varphi_s = E_g/2 + kTx_n = -E_g/2 - kTx_p$, and q_L is the mobile charge per unit length, including both electrons and holes. Applying Eqs. (8) and (9) for the charge densities, C_q is derived as

$$C_{q\_n} = \sum_{q=1}^{2} \frac{e^2 n(q)}{kT}\left\{1 - \frac{[2N_0 e^{x_n} - n(q)](\alpha + 2\beta x_n + 3\gamma x_n^2)}{2N_0 e^{x_n}}\right\}, \tag{11a}$$

$$C_{q\_p} = \sum_{q=1}^{2} \frac{e^2 p(q)}{kT}\left\{1 - \frac{[2N_0 e^{x_p} - p(q)](\alpha + 2\beta x_p + 3\gamma x_p^2)}{2N_0 e^{x_p}}\right\}, \tag{11b}$$

which simplifies to the nondegenerate quantum capacitance when $2N_0 \exp(x_n) = n$ or $2N_0 \exp(x_p) = p$.[20]

Figure 4 plots the low energy analytical quantum capacitance for the electrons and holes at room temperature, showing a remarkably good agreement compared with numerical tight-binding computation. It is worth mentioning that the sharp increase in C_q corresponds to the occupation of a subband, and the peaks reflect the VHS in the DOS. Beyond the singularities, the DOS decays, causing a slow decrease in C_q until the occupation of next subband. In order to quantitatively evaluate the comparison, we introduce the average error which is the mean value of the difference between Eq. (11) and the NNTB computation. The average error is 2.8%, 3.9%, and 4.3%, for 1nm, 1.5nm, and 2nm CNTs, respectively. These low errors make the semiempirical analytical model useful in place of numerical computation.

We further employ the analytical quantum capacitance in the lumped circuit C-V model[9,20] of a top-gated CNT as shown in Fig. 5. At quasistatic frequencies and low temperatures, the lumped model simplifies to two series capacitors. Therefore, the total gate capacitance C_{tot} is

$$C_{\text{tot}}(V_g) = \frac{C_{\text{tg}} C_q(\varphi_s)}{C_{\text{tg}} + C_q(\varphi_s)}, \tag{12}$$

where V_g is the applied gate voltage and C_{tg} is the top-gate oxide capacitance. The surface potential φ_s is determined from the capacitive divider network (assuming zero flatband voltage):

$$\varphi_s = \frac{C_{\text{tg}}}{C_{\text{tg}} + C_q(\varphi_s)} V_g, \tag{13}$$

which is an implicit function coupled with the calculation of C_q from Eq. (10). For a given V_g, φ_s can only be solved by self-consistent iteration and hence, C_{tot} is computed semianalytically in the lumped C-V model. Figure 6 shows the comparison of the semianalytical C-V model, numerical compu-

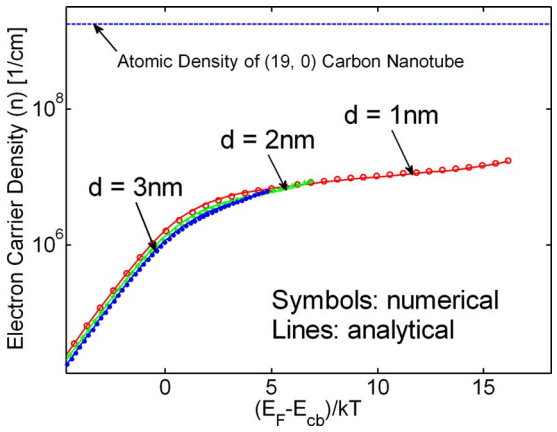

FIG. 3. (Color online) Comparison between analytical electron carrier density [Eq. (8)] and numerical solution for the electron carrier density at room temperature with good agreement (error within 5%). The dashed line shows the atomic density of (19, 0) zigzag CNT for reference.

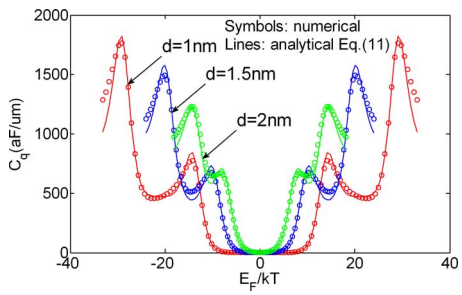

FIG. 4. (Color online) The quantum capacitance [analytical model Eq. (11) and NNTB computation] for sCNTs, which includes the contribution of both electrons and holes, as a function of the Fermi level at room temperature. The average error is 2.8% for a 1 nm CNT, 3.9% for a 1.5 nm CNT, and 4.3% for a 2 nm CNT.

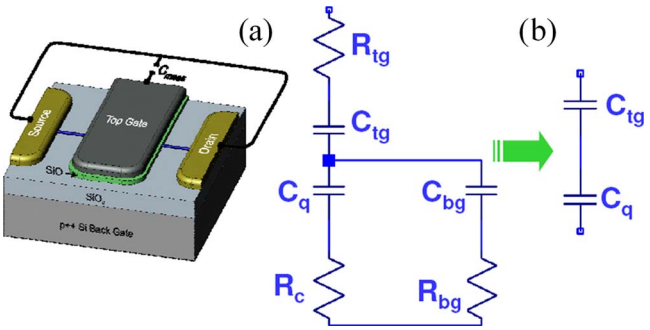

FIG. 5. (Color online) (a) Optimized top-gated CNT device [figure and data courtesy of Ilani *et al.* (Ref. 9)] for attofarad capacitance measurements using a 20 aF resolution capacitance bridge. (b) Lumped circuit model of the top-gated CNT device. R_{tg} and C_{tg} are the top-gate metal resistance and gate oxide capacitance. C_{bg} and R_{bg} are the back-gate substrate resistance and capacitance, and R_c is the contact resistance to the CNT. The left schematic is the general model including resistances and capacitances which simplifies to a series connection of the gate oxide and quantum capacitances valid at low frequencies and low temperature (Ref. 12).

tation and C-V measurement[9] at 77 K with good agreement. The discrepancy at the bottom of the curve is due to the resolution of the capacitance bridge while the deviation at the first subband peak has been reported to be due to electron correlations,[9] which are not captured in the independent electron tight-binding formalism.

It is desirable to avoid the self-consistent numeric iteration for the solution of the C-V model, in order to evaluate C_q and φ_s algebraically from the applied voltage. To achieve this, a straightforward relation between φ_s and the external gate voltage is not only necessary, but also useful for intuitive understanding and compact modeling. An illustrative surface potential as a function of V_g for a CNT with diameter=2.5 nm (for the device in Fig. 5) is shown in Fig. 7. We can see that φ_s saturates with V_g and is pinned $\sim E_g/2e$ at high V_g due to the large DOS at $E_g/2e$. This means that practical Fermi level in sCNTs is largely restricted to the bottom of the first subband, which validates the proposed

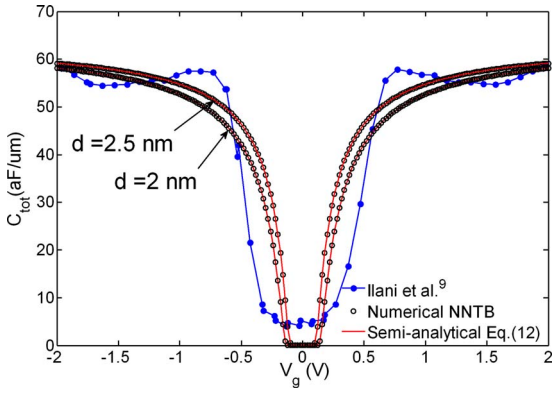

FIG. 6. (Color online) The total gate capacitance vs top-gate voltage of the CNT device in Fig. 5. The measurement, simulation, and model using Eq. (12) are all performed at 77 K and 1 KHz. The NNTB computation and semianalytical C-V model both use CNT diameters of 2 nm and 2.5 nm, within the 2.5 nm ± 0.5 nm atomic force height of the experimental CNT. A gate oxide capacitance of 64 aF/um was used which is close to the wire over plane estimate of 72 aF/um. An excellent match can be observed between semianalytical model and numerical computation, and they are both in strong agreement with the measured data.

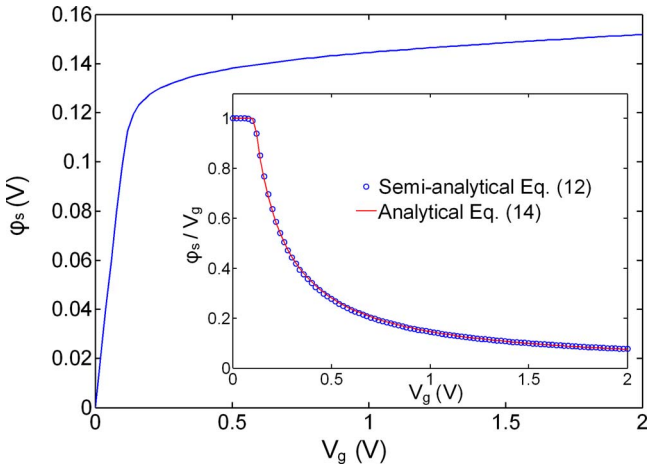

FIG. 7. (Color online) Surface potential φ_s as a function of V_g for a CNT diameter of 2.5 nm ($E_g \sim 0.31$ eV) at 77 K. φ_s eventually saturates and is pinned around $E_g/2e$ at high V_g. The inset shows the gate coupling function versus top-gate voltage illustrating how the gate voltage couples to the CNT. At low V_g, the gate voltage couples completely to the CNT, and at high V_g, the gate gradually loses control of the CNT surface potential. The analytical gate coupling function [Eq. (14)] fits the semianalytical C-V model [Eq. (12)] with a peak error of 1.8%.

two-subband approximation. This is further demonstrated by the gate coupling function φ_s/V_g in the inset of Fig. 7, which quantifies how strongly the gate couples to the CNT. For low V_g ($<E_g/2e<0.15$ V), φ_s is very small and the quantum capacitance is several magnitudes smaller than C_{tg}. Hence, the gate couples completely and controls the surface potential linearly with a slope of ~unity. However, at higher voltages the external gate voltage gradually loses control of the surface potential because the CNT becomes increasingly metallic-like.

We can see from the inset of Fig. 7 that φ_s/V_g is well approximated by two components: 1) a constant one when V_g is small, and 2) a decaying quasiexponential at high V_g. A two-parameter analytical equation for φ_s/V_g is thus obtained and compared to the semianalytical C-V model with a peak error of 1.8% in the inset of Fig. 7:

$$\frac{\varphi_s}{V_g} = 1 - \left(1 - \frac{1}{s|V_g| + t}\right) H\left(1 - \frac{1}{s|V_g| + t}\right), \tag{14}$$

where $H(\cdot)$ is the Heaviside unit step function. For the specific case considered in Fig. 7, $s=6.75$ and $t=0.27$. It is obvious from Eq. (14) that when the step function is zero (the quantum capacitance limit), φ_s/V_g reduces to 1, and when the step function is unity, φ_s/V_g reduces to $1/(sV_g+t)$, which takes the form of the decaying part in the inset of Fig. 7.

It is worth mentioning that the results we have obtained based on the zigzag sCNTs are readily applicable to semiconducting chiral CNTs with similar diameters.[13,14] This is because of the strong diameter dependence of the CNT band structure at low energies. At high energies, the gate oxide capacitance dominates over the quantum capacitance, which suppresses any capacitance differences among diverse sCNTs of similar diameters.

IV. CONCLUSION

In this paper, we have developed an analytical carrier density and quantum capacitance using a semiempirical method for arbitrary positions of the Fermi level up to the bottom of the second subband, showing a strong agreement with numerical tight-binding computation. A C-V model of a top-gated CNT is presented based on the analytical quantum capacitance with good correlation with experimental data. In addition, we have presented an analytical gate coupling function which is very accurate in quantifying how strongly the gate controls the CNT surface potential and carrier density. In practical CNT transistors, the Fermi level hardly goes beyond the bottom of the conduction band of the first subband due to the sharp increase in the quantum capacitance with applied gate voltage.

The developed analytical carrier density and quantum capacitance captures the diameter, temperature, and Fermi level dependence and offers insight into the essential device physics of CNTs both qualitatively and quantitatively. These results lay the foundation for formulating analytical equations for describing the transport (*I-V* characteristics) and compact modeling of CNT devices, and for diameter optimization of CNT for maximum electrical performance.

ACKNOWLEDGMENTS

This work was supported in part by the Focus Center Research Program (FCRP) Center for Circuit and System Solutions (C2S2). J.L. was additionally supported by Gerald L. Pearson Memorial Fellowship. D.A. was additionally supported by the Ford foundation and Alfred P. Sloan graduate fellowships.

APPENDIX

The characteristics and accuracy of the analytical carrier density model whose highest order in the exponential series is up to two for the two subbands are given in Table II, showing an acceptable accuracy especially for the high *dT* and medium *dT* region.

TABLE II. The characteristics and accuracy of the analytical model (up to two orders). The optimal values of A and weight parameters α and β for three regions are chosen to minimize the peak error for all regions. The high *dT* region is the only relevant region for practical CNTs with diameters from 1 to 4 nm operating at room temperature.

dT (nm·K)	Fitting weights α	Fitting weights β ($\times 10^{-3}$)	A	Peak error
70–150	0.94	0.46	0.52	14.5%
150–220	0.91	1.35	0.60	6.5%
220–1500	0.88	2.41	0.63	5.7%

[1] S. Iijima and T. Ichihashi, Nature (London) **363**, 603 (1993).
[2] A. Javey, J. Guo, D. B. Farmer, Q. Wang, E. Yenilmez, R. G. Gordon, M. Lundstrom, and H. J. Dai, Nano Lett. **4**, 1319 (2004).
[3] M. S. Purewal, B. H. Hong, A. Ravi, B. Chandra, J. Hone, and P. Kim, Phys. Rev. Lett. **98**, 186808 (2007).
[4] H. Kataura, Y. Kumazawa, Y. Maniwa, I. Umezu, S. Suzuki, Y. Ohtsuka, and Y. Achiba, Synth. Met. **103**, 2555 (1999).
[5] J. Li, Y. Lu, Q. Ye, M. Cinke, J. Han, and M. Meyyappan, Nano Lett. **3**, 929 (2003).
[6] N. W. Ashcroft and N. D. Mermin, *Solid State Physics* (Holt, Rinehart, and Winston, New York, 1976).
[7] J. Guo, A. Javey, H. Dai, and M. Lundstrom, Tech. Dig. - Int. Electron Devices Meet. **2004**, 703.
[8] D. Akinwande, Y. Nishi, and H.-S. P. Wong, IEEE Trans. Electron Devices **55**, 289 (2008).
[9] S. Ilani, L. A. K. Donev, M. Kindermann, and P. L. McEuen, Nat. Phys. **2**, 687 (2006).
[10] J. Deng and H.-S. P. Wong, IEEE Trans. Electron Devices **54**, 3195 (2007).
[11] K. Natori, Y. Kimura, and T. Shimizu, J. Appl. Phys. **97**, 034306 (2005).
[12] A. Raychowdhury, S. Mukhopadhyay, and K. Roy, IEEE Trans. Comput.-Aided Des. **23**, 1411 (2004).
[13] J. W. Mintmire and C. T. White, Phys. Rev. Lett. **81**, 2506 (1998).
[14] C. T. White and J. W. Mintmire, Nature (London) **394**, 29 (1998).
[15] O. Gülseren, T. Yildirim, and S. Ciraci, Phys. Rev. B **65**, 153405 (2002).
[16] R. Saito, G. Dresselhaus, and M. S. Dresselhaus, *Physical Properties of Carbon Nanotubes* (Imperial College, London, 1998).
[17] S. Reich, C. Thomsen, and J. Maultzsch, *Carbon Nanotubes: Basic Concepts and Physical Properties* (Wiley, Weinheim, Cambridge, 2004).
[18] P. Jarillo-Herrero, S. Sapmaz, C. Dekker, L. P. Kouwenhoven, and H. S. J. van der Zant, Nature (London) **429**, 389 (2004).
[19] D. L. John, L. C. Castro, and D. L. Pulfrey, J. Appl. Phys. **96**, 5180 (2004).
[20] D. Akinwande, Y. Nishi, and H.-S. P. Wong, Tech. Dig. - Int. Electron Devices Meet. **2007**, 753.